Equation of State and Transport Property Measurements of Warm Dense Matter

Marcus D. Knudson

Sandia National Laboratories

Equation of State and Transport Property Measurements of Warm Dense Matter

Marcus D. Knudson and Michael P. Desjarlais
Dynamic Materials Properties Group

Sandia National Laboratories
P.O. Box 5800
Albuquerque, NM 87185-1195

Abstract

Location of the liquid-vapor critical point (c.p.) is one of the key features of equation of state models used in simulating high energy density physics and pulsed power experiments. For example, material behavior in the location of the vapor dome is critical in determining how and when coronal plasmas form in expanding wires. Transport properties, such as conductivity and opacity, can vary an order of magnitude depending on whether the state of the material is inside or outside of the vapor dome. Due to the difficulty in experimentally producing states near the vapor dome, for all but a few materials, such as Cesium and Mercury, the uncertainty in the location of the c.p. is of order 100%. These states of interest can be produced on Z through high-velocity shock and release experiments. For example, it is estimated that release adiabats from ~1000 GPa in aluminum would skirt the vapor dome allowing estimates of the c.p. to be made. This is within the reach of Z experiments (flyer plate velocity of ~30 km/s). Recent high-fidelity EOS models and hydrocode simulations suggest that the dynamic two-phase flow behavior observed in initial scoping experiments can be reproduced, providing a link between theory and experiment. Experimental identification of the c.p. in aluminum would represent the first measurement of its kind in a dynamic experiment. Furthermore, once the c.p. has been experimentally determined it should be possible to probe the electrical conductivity, opacity, reflectivity, etc. of the material near the vapor dome, using a variety of diagnostics. We propose a combined experimental and theoretical investigation with the initial emphasis on aluminum.

Acknowledgements

Contents

This page intentionally left blank

1. Introduction

One of the key features of equation of state (EOS) models for simulating high energy density physics and pulsed power experiments is the location of the liquid-vapor critical point (c.p.). Of particular interest is the conductivity of the material in this vapor dome region of the EOS surface. For example, knowledge of the conductivity in and around the vapor dome is critical in determining how and when coronal plasmas form in expanding wires. Transport properties, such as the conductivity and opacity, can vary an order of magnitude depending on whether the state of the material is within or outside the vapor dome.

The location of the c.p. is difficult to ascertain. In fact, the c.p. has only been experimentally measured for a few materials such as Cesium and Mercury. For other materials, the uncertainty in the location of the vapor dome is of order 100%. The reason for this is two-fold. First, experimentally this is a very difficult region of the EOS surface to access, at least in a well-defined, uniform state. Second, this region has traditionally been of lesser importance to theorists, and therefore the details of this portion of the EOS surface have not been emphasized.

The flyer plate capability on the Z accelerator provides a means of accessing this region of the EOS surface. Through appropriately defined shock and release experiments it may be possible to create well-defined, uniform states near the c.p. Adiabatic release from several 100 GPa Hugoniot states results in material at near ambient densities and high temperatures (e.g. aluminum at ~0.5 g/cc and 10000 K), in the vicinity of the c.p. (current estimates of the c.p. for aluminum is ~1/8-1/5 solid density and ~6000 K [1-4]). Furthermore, the relatively large sample sizes and number of samples that can be nearly identically loaded in flyer plate experiments on Z enable a variety of diagnostics to be used to interrogate the shock and release states.

Experimental identification of the c.p. in aluminum would be a significant achievement. In fact, it would represent the first measurement of its kind in a dynamic experiment. Furthermore, once the c.p. has been established, it may be possible to probe the transport properties of the plasma (electrical conductivity, opacity, reflectivity, etc.) near the vapor dome using various diagnostic techniques that will be outlined below.

We chose to use the high flyer plate velocities achievable on Z to perform shock and release experiments to access the EOS region of interest. The advantage of using Z for this purpose is that macroscopic samples can be created given the relatively large size of the flyer plates and targets. Furthermore, since two flyers are launched, multiple samples could be created in a single firing of the accelerator. This allowed (i) the ability to utilize several similar measurements on a single experiment, thereby increasing the accuracy of any given measurement and (ii) the ability to field different diagnostics on the same experiment, thereby enabling consistency checks to be made, resulting in more confidence in the interpretation of the data.

We performed a feasibility study on aluminum. Work on aluminum allowed us to leverage the significant amount of data that has been obtained on the shock and release response of aluminum [5,6]. Although aluminum is one of the most widely studied metals, there is still significant uncertainty in the location of the vapor dome, as well as the nature of the material around the vapor dome. Fig. 1.1 shows release adiabats in density-temperature-pressure space from
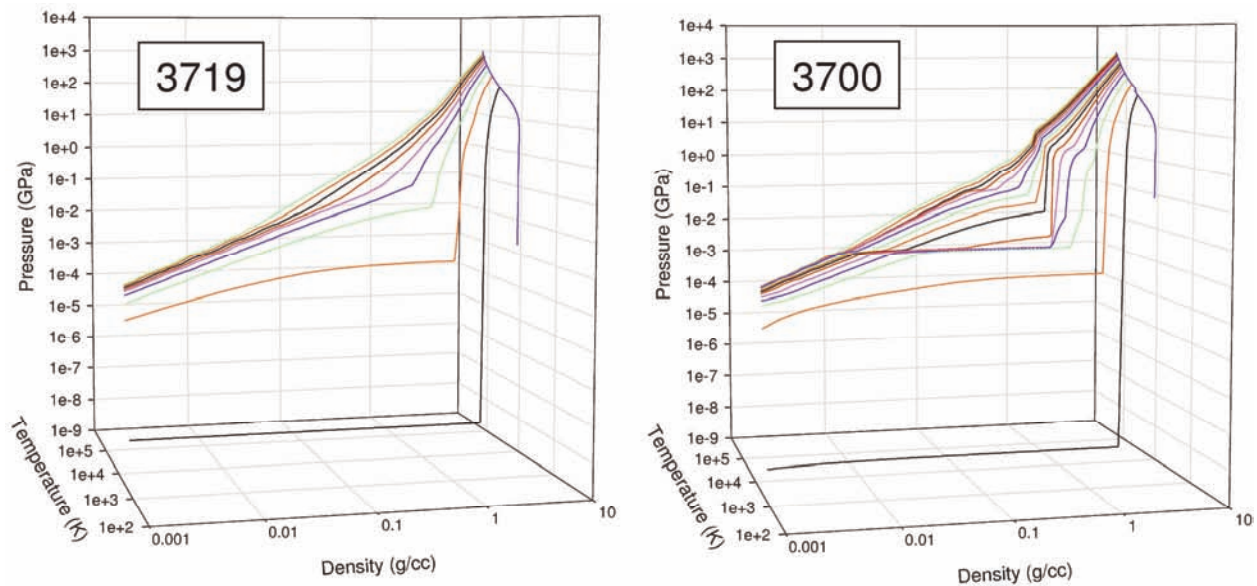
Figure 1.1. Release isentropes from Hugoniot states ranging in pressure from 100-1000 GPa for SESAME 3719 (left) and 3700 (right). For both plots the blue line is the Hugoniot.

Hugoniot states for two different, widely used models for aluminum, SESAME 3719 [1] and 3700 [2]. Notice the significant difference in the behavior near the vapor dome. In particular, SESAME 3700 predicts a metal-insulator transition at temperatures just above the critical point, while 3719 does not.

Fig. 1.2 shows projections release isentropes in the temperature-density plane for SESAME 3700 and 3719 along with two additional models, SESAME 3711 [3] and 3720 [4]. Notice the significant difference in the release isentropes that skirt the cp. In particular 3719 predicts release from ~500-600 GPa on the Hugoniot will skirt the cp; 3720 predicts ~800-900 GPa is needed; 3711 predicts a Hugoniot state over 1000 GPa is necessary. The predicted metal-insulator transition in SESAME 3700 confounds the determination of a release isentrope that skirts the cp. To date there has been no experimental evidence to either support or refute this proposed transition. Furthermore, no experimental evidence exists to suggest which of the other models, 3711, 3719, or 3720, is more accurate if this proposed transition does not exist.

This study focused on exploring release adiabats from high-pressure Hugoniot states in an attempt to bracket the adiabats that skirt the c.p. of the vapor dome. Three different experimental concepts were pursued. The first of these was full release experiments. In these experiments, high velocity aluminum flyer plates impacted a stationary aluminum target. The induced shock wave transited the target and fully released into a vacuum. The release of the material was then probed in an attempt to infer the density profile of the aluminum as it expanded. The second experimental concept was optical shadowgraphy and x-ray backlighting. These experiments were similar to the full release experiments in that aluminum flyer plates struck stationary aluminum targets which released into a vacuum. However, for these experiments a high density screen was used in an attempt to limit the width of the expanding plasma such that optical and x-ray photons could be used to interrogate the density profile of the plasma. The third experimental concept was tamped release experiments. In these experiments the shocked aluminum target was the front
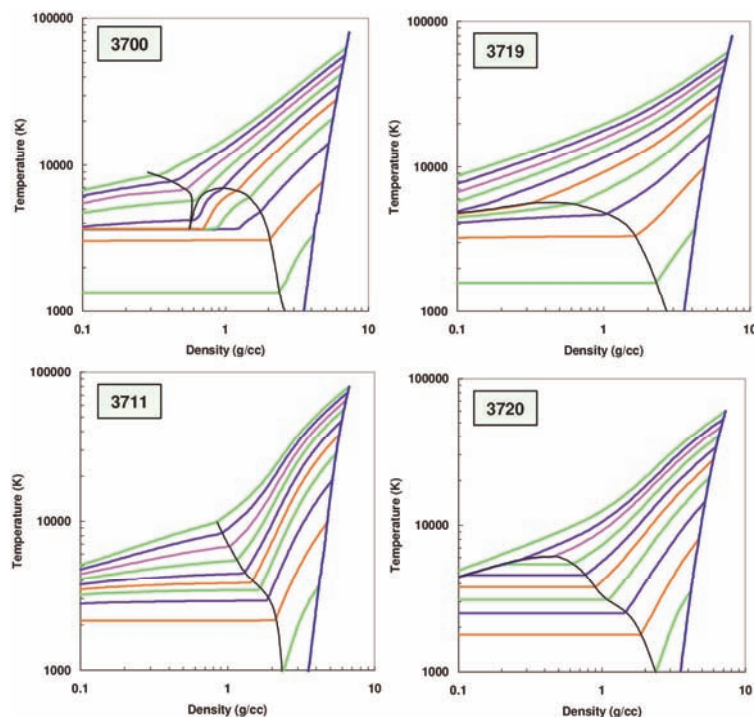
Figure 1.2. Release isentropes in the temperature-density plane from Hugoniot states ranging in pressure from 100-1000 GPa for SESAME 3700, 3719, 3711, and 3720. For all plots the nearly vertical blue line is the Hugoniot.

plate of a gas cell containing a low density gas. The gas prevented the aluminum from releasing to zero pressure. Rather the gas tamped the release at pressures near ~0.1 GPa, below the various predictions for the pressure of the liquid-vapor critical point. The response of the gas was then observed in an attempt to observe a signature of release near the critical point. Each of these experimental concepts are discussed in the following three sections.

Concurrently, a theoretical investigation of aluminum was performed using quantum molecular dynamics (QMD) methods. In particular QMD calculations were performed in an attempt to determine the pressure, temperature, and density of the liquid-vapor critical point. Once the critical point was determined QMD methods were also used to estimate the pressure state on the Hugoniot that would

release near the critical point. Finally, QMD calculations were performed to provide key input for development of a Quotidian equation of state (QEOS) type, global EOS model for aluminum that was much more finely resolved in the vapor dome region than typical EOS models for aluminum found in the SESAME library. Discussion of the QMD calculations and the QEOS model is found in Section 5.

2. Full Release Experiments

The initial experimental campaign focused on full release experiments, mainly due to intriguing results obtained in earlier full release experiments performed on Z. The experimental configuration is quite simple, and is illustrated in Fig 2.1. An aluminum flyer plate, 17 mm by 40 mm by initially 850 microns in thickness, is magnetically accelerated to velocities ranging from ~14-25 km/s. These plates impact stationary aluminum targets, typically 300 microns in thickness. A LiF witness plate is placed a distance of 1 mm behind the aluminum target. The impact induced shock wave transits the aluminum target and is reflected at the rear surface as a rarefaction wave that propagates back toward the impact side of the target releasing the aluminum to zero pressure. This results in an expansion of the high temperature, low density material toward the LiF witness plate.
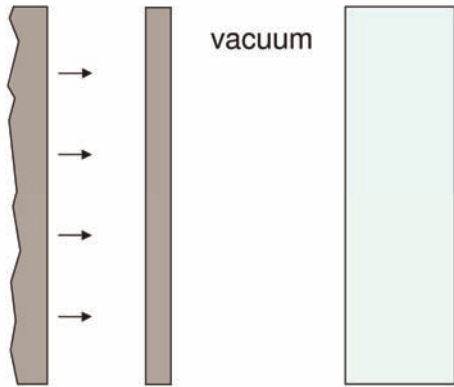
vacuum

Figure 2.1. Experimental configuration for the full release experiments.

These experiments utilized a single point velocity interferometer (VISAR [7], Velocity Interferometer System for Any Reflector), a line-imaging VISAR, or a temporally and spectrally resolved diagnostic. Typical data from the line-imaging VISAR and the spectrally and temporally resolved diagnostic are shown in Fig 2.2. In both cases the shock arrival at the rear surface of the aluminum is observed through the loss of reflected laser from the target. Very little light is observed after shock break out until the time that low density plasma reaches the LiF witness plate. The arrival of the low density plasma is apparent as a rapid increase in light emission. As can be seen in the lower portion of Fig. 2.2, this emission is across the entire visible spectrum and is due to heating of the plasma as it stagnates at the LiF witness plate. Given the known distance between the aluminum target and LiF witness plate, the velocity of the expanding plasma can be determined.

In all of the experiments performed of this type, a second burst of emission was observed. Previous aerogel experiments performed on Z suggest that this second burst of emission originates from the LiF witness plate (see Fig. 3 from Ref. [6]). We speculate that this burst of emission is caused by a rather strong shock in the LiF witness plate. This could only result from a distinct and sharp density increase in the expanding aluminum. Such a feature would be expected if the release adiabat entered the vapor dome. Under this scenario, the leading edge of the aluminum release would correspond to a rapidly expanding, low density aluminum vapor. At some distance behind this leading edge would be a somewhat lower expanding, transition region from vapor to liquid, with a corresponding sharp increase in the density profile. Again, given the known distance between the aluminum target and the LiF witness plate, the velocity of the liquid front can also be determined.

A compilation of the experimental results are shown in Fig. 2.3. Given the symmetric nature of the impact experiment, the particle velocity is simply one half of the measured flyer plate velocity. The expansion velocity is defined to be the additional velocity of the expanding vapor or liquid front with respect to the impact velocity. In the absence of thermal effects, one would expect the velocity of the aluminum
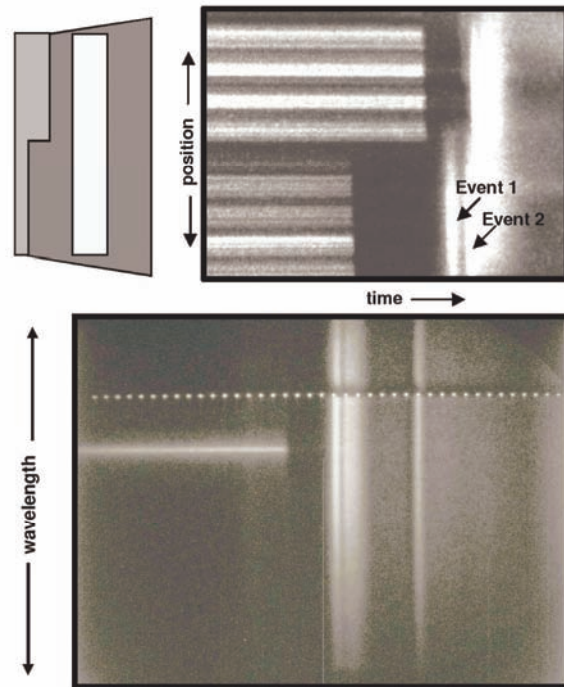

Figure 2.2. Typical experimental data obtained from full release experiments. Top panel shows line-imaging VISAR data, while the bottom panel shows spectrally and temporally resolved data. The dotted line in the bottom panel is a time fiducial.
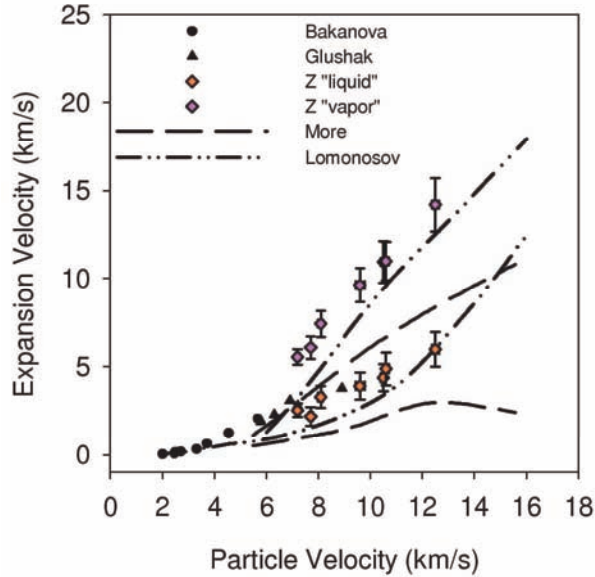
Figure 2.3. Expansion velocity as a function of particle velocity of aluminum in the shocked state. Pink (orange) diamonds are the measured vapor (liquid) front velocities. Also shown are data from Bakanova and Glushak and theoretical predictions from Lomonosov and More.

release to be twice the particle velocity, or equivalently the impact velocity. Thus the expansion velocity gives an indication of the additional velocity imparted to the expanding aluminum due to thermal effects which include melting and vaporization.

The measured expansion velocities of the leading edge of the vapor as a function of the particle velocity of the aluminum in the shocked state are shown as pink diamonds in Fig. 2.3. The measured expansion velocities of the expanding liquid front are shown as orange diamonds. Also shown in the figure are measured expansion velocities from similar experiments performed by Bakanova [8] and Glushak [9]. Their experiments differed in one significant aspect; the aluminum did not fully release, but was tamped by one atmosphere of air. Bakanova and Glushak concluded that the tamping resulted in stagnation pressures of ~7 kbar, which prevented the release adiabat from entering the vapor dome. Thus their experiments did not exhibit a vapor component, and their results should therefore be compared with our expansion velocity of the proposed liquid front. Finally, two theoretical predictions are shown in Fig 2.3, obtained from EOS models developed by Lomonosov [10] and More [11]. We note that the EOS model from More is an earlier version of the QEOS model to be discussed in Section 5.

As can be seen in Fig 2.3, reasonable agreement is seen between the liquid front velocities and the expansion velocities reported by Bakanova and Glushak. Also, reasonable agreement is observed between the Z experiments and the predictions of Lomonosov. This is not entirely unexpected, given the fact that the Lomonosov model used the data of Bakanova and Glushak in its development. The comparison with the predictions of More are not as good, however we reiterate that this is an earlier version of his QEOS. We have not been able to make similar comparisons with his most recent version which is discussed in Section 5.

It is clear from the experimental results that the second feature was observed over the entire pressure range investigated, ~300-700 GPa (corresponds to impact velocities of ~14-25 km/s). This would suggest that release adiabats from these pressure states along the Hugoniot all enter the vapor dome upon release.

3. X-ray Backlighter and Shadowgraphy Experiments

At this point we began an experimental campaign in an attempt to directly measure the density profile of the expanding aluminum using x-ray backlighting and optical shadowgraphy techniques. The experimental configuration for these experiments is shown in Fig 3.1. The
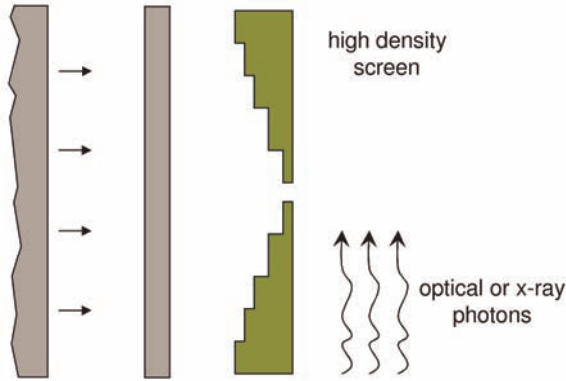
Figure 3.1. Experimental configuration for the x-ray backlighter and optical shadowgraphy experimetns. The view is looking down from the top; the side view of the screen would have a similar profile with a larger opening.

concept is similar to the full release experiments, with the LiF witness plate replaced by a high density screen. The idea being that the high density screen would act to create a "ribbon" of expanding aluminum with a width such that the x-ray backlighter, a 6.1 kV curved crystal imiaging system [12], could penetrate and provide a measure of the density profile.

To determine the appropriate width given the available backlighter energy, highly resolved 1D hydrocode simulations were performed using CTH. It was found that cell size in the vacuum region needed to be on the order of ~0.1 micron to obtain adequate resolution to observe a distinct liquid-vapor transition region at lower pressures. This resulted in very long computational time given that the aluminum needed to expand over a distance of 1 mm. Results of several simulations, using SESAME 3719 for the aluminum EOS, are shown in Fig. 3.2. Release calculations were performed from 300, 500, and 800 GPa. Given
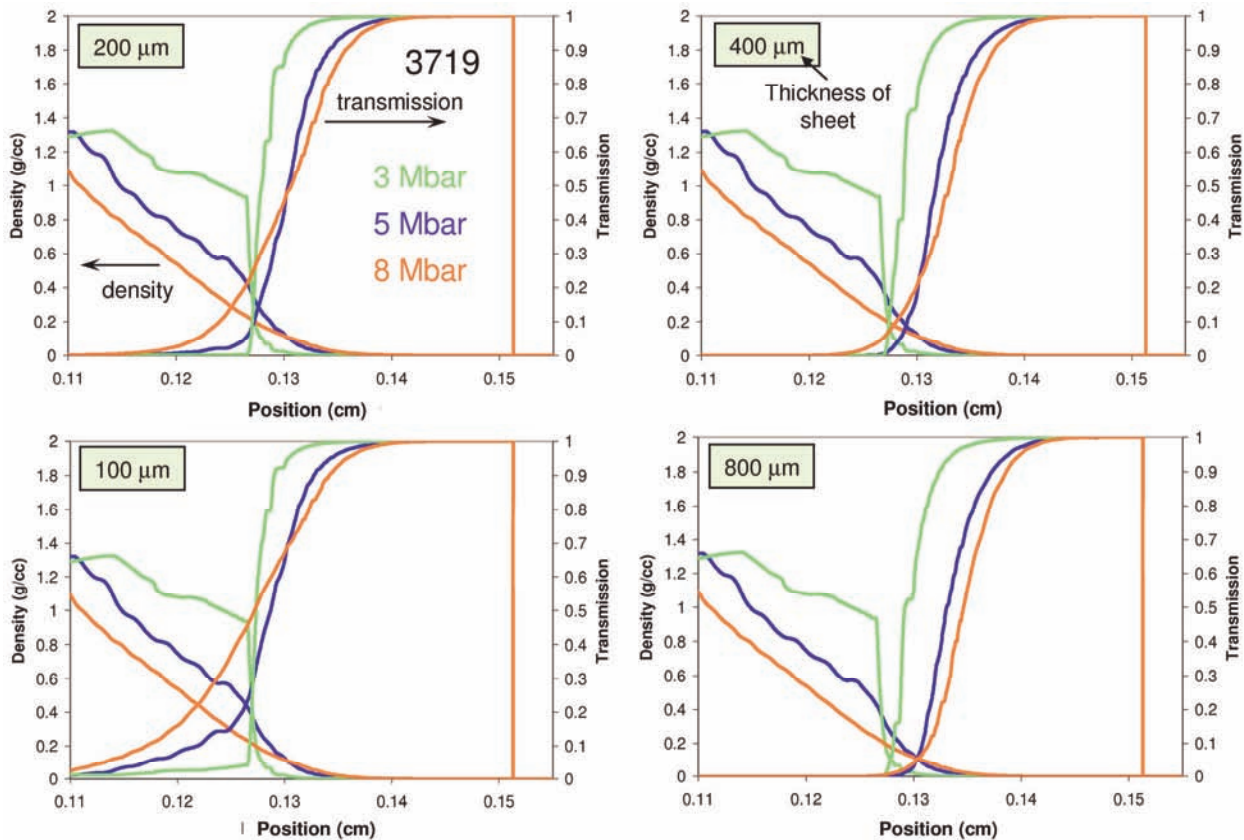

Figure 3.2. Results of 1D CTH simulations of aluminum release. Shown are the predicted transmission profiles for four different thickness screens, indicating that widths of ~100 microns are necessary to observe details regarding the liquid-vapor transition. Note 1 Mbar = 100 GPa
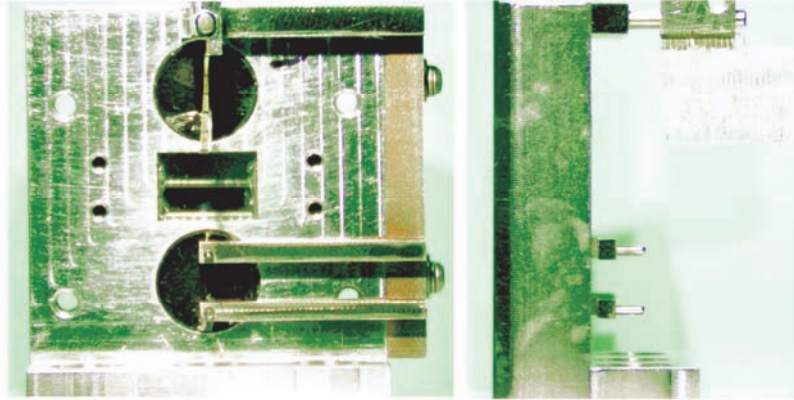
12

Figure 3.3. Experimental hardware used in the x-ray backlighter and optical shadowgraphy experiments. Left (ride) side show view perpendicular (parallel) to the photon path.

the transmission of aluminum to 6.1 kV energy photons, the transmission through various thickness "sheets", determined by various width screens, could be determined. Fig. 3.2 shows the calculated density profiles and corresponding x-ray transmission profiles for four different width screens ranging from 100 to 800 microns.

In order to be able to distinguish fine details regarding the liquid-vapor transition with this x-ray backlighter energy the screen width needed to be quite small. As can be seen in Fig 3.2, even with a screen width of 100 microns the transmission through the liquid region of the 300 GPa release density profile is predicted to be only a few percent. This motivated our choice of 50-200 micron screen widths for subsequent experiments. The height of the screen was 5 mm.

An example of the actual experimental hardware is shown in Fig 3.3. The left side of the figure shows the rear of the flyer plate panel. The top circular sample area shows the tungsten screen used in the x-ray backlighter experiment, the bottom circular sample area shows the tungsten screen used in the optical shadowgraphy experiment. The central rectangular sample area is comprised of quartz windows to enable the flyer velocity to be measured using VISAR diagnostics. The right side of Fig. 3.3 shows a side on view of the flyer plate panel, a view which is parallel to path of the x-ray and optical photons during the experiment. This view shows the screen (top) and pins (bottom) used as spatial fiducials for the diagnostics.

Unfortunately, no usable x-ray backlighter data was obtained from 3 individual Z experiments. We did, however, obtain optical shadowgraphy data from all experiments. In these experiments a side view of the rear of the flyer plate panel (i.e. right side of Fig. 3.3) was imaged onto the input of a fast framing camera capable of recording 6 individual frames, each with ~2 ns exposure

Figure 3.4. Experimental data from a shadowgraphy experiment. Shown are five frames, each with ~2ns exposure, timed ~15 ns apart. Clearly evident is an expanding aluminum plasma.

time, with variable time between frames. Typical interframe times were of order 15 ns. An expanded laser beam was used as a light source for the experiment, which essential records a shadow of the projected image. Typical data from a shadowgraphy experiment is shown in Fig. 3.4. Clearly evident in the series of framing camera images is an expansion of aluminum. Because this is optical photons, the diagnostic can only determine the leading edge of the expanding aluminum, no details of the density profile behind the edge can be determined. The spatial fiducials provide a means of determining the expansion velocity of the leading edge.

Figure 3.5. Expansion velocity as a function of particle velocity of aluminum in the shocked state. Green diamonds are results inferred from shadowgraphy experiments.

The resulting expansion velocities are shown in Fig. 3.5 along with the data from the full release experiments. The shadowgraphy results are suggestive of a rapid increase in the expansion velocity of the vapor component at a particle velocity of ~12 km/s, corresponding to ~700 GPa. This behavior is in stark contrast to the predictions of Lomonosov. At first this was believed to be evidence for the location of the critical point. It was

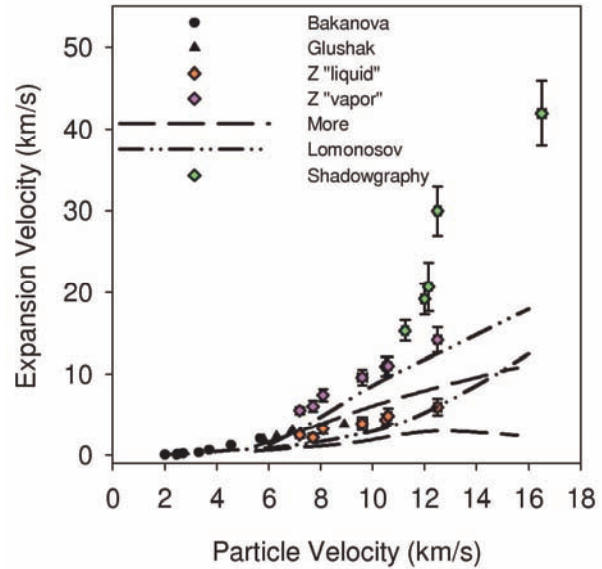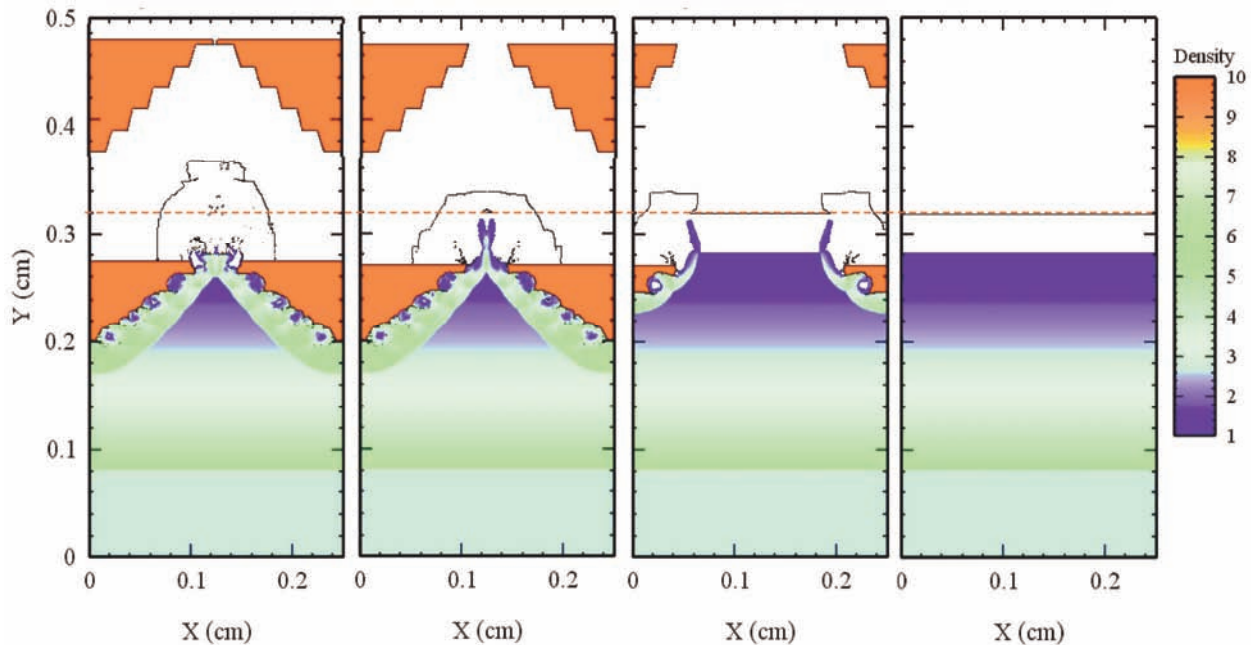Figure 3.6. Snapshots from four finely resolved 2D CTH simulations showing the effects of material jetting due to interaction of the expanding aluminum with the tungsten screen. Screen width openings are (left to right) 50 microns, 200 microns, 1.3 mm, and semi-infinite.
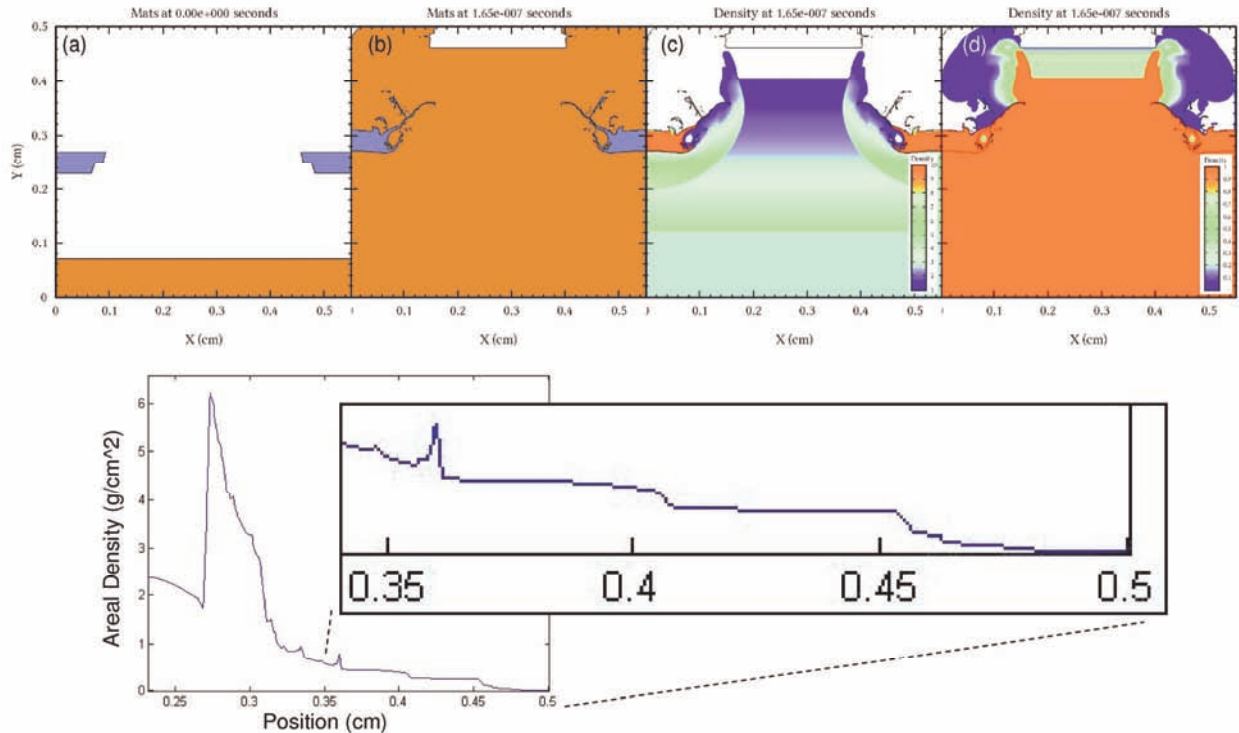
14

Figure 3.7. Snapshots from a finely resolved 2D CTH simulation for a screen width opening 3.5 mm. The resulting material jetting does not collide. Bottom panel shows an integrated areal density plot showing that the density increase at the liquid-vapor transition, which occurs at a position of ~0.4 cm, is still evident.

thought that the for release above ~700 GPa the adiabat skirted over the top of the vapor dome, resulting in a rapid increase in the expansion velocity of the vapor. However, this interpretation was also viewed with caution given that fact that the measurements at lower pressure that are in reasonable agreement with the predictions of Lomonosov were obtained using a different experimental configuration.

To test the hypothesis it was decided that an additional full release experiment be performed at higher impact velocities to compare with the shadowgraphy results. An experiment was performed at an impact velocity of ~26 km/s. The resulting expansion velocity measurement is shown in Fig. 3.5. The result of this experiment was consistent with the lower pressure full release experiments, in reasonable agreement with the prediction of Lomonosov, and significantly lower than the expansion velocity inferred from the shadowgraphy experiment.

This inconsistency suggested that some experimental artifact was potentially affecting the shadowgraphy experiment. To determine a possible cause we performed very finely resolved 2D simulations of the interaction of the expanding aluminum with the tungsten screen using CTH. A series of simulations were performed for various width screens; snapshots from these simulations are shown in Fig. 3.6.

The original screen design used several layers of tungsten with systematically decreasing opening widths such that the width diminished from ~2 mm to ~50 microns over a thickness of 1
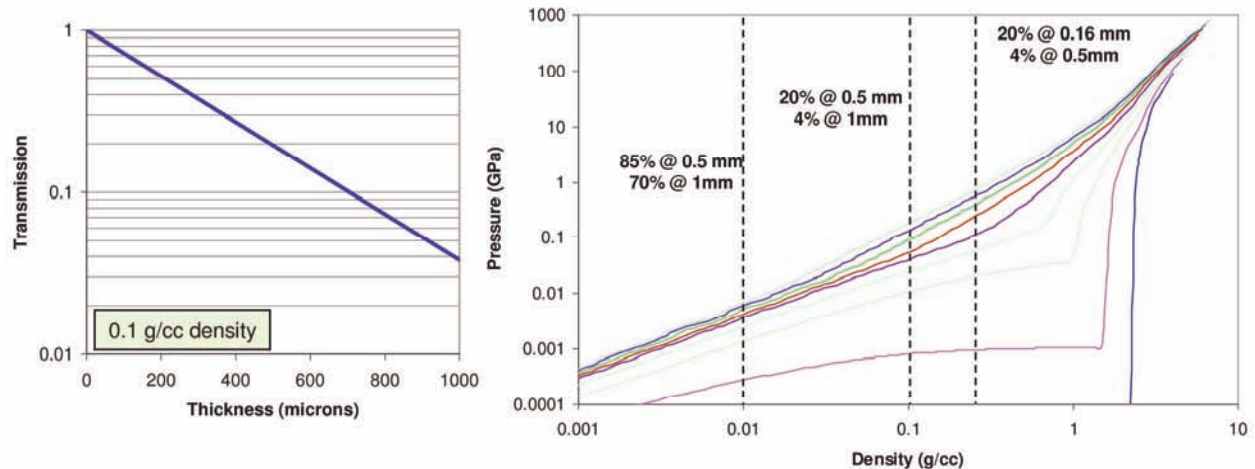
Figure 3.8. Expected transmission through expanded aluminum for a 25 kV backlighter. Note that reasonable transmission is expected for densities near the expected critical point.

mm. This was done in an attempt to mitigate 2D effects in the aluminum/screen interactions. It is evident from the snapshots shown in Fig 3.6 that the 2D effects were significant, and that the leading edge of the expansion is accelerated do to these interactions. Furthermore, the acceleration is enhanced for screen widths below ~300 microns due to the collision of jets formed by the interaction of the aluminum and the edge of the screen opening. Given that the screen openings in the experiments were all 200 microns or less, these calculations suggest that the enhanced expansion velocity was due to material jetting.

Consequently, larger screen size openings would be needed to minimize jetting issues. Unfortunately that would preclude the use of a 6.1 kV backlighter as a diagnostic. At the time of this study there was an ongoing effort to develop a 25 kV backlighter for the Z PetaWatt project. A higher energy backlighter would enable x-ray penetration through more material. We thus began design of an experiment that could utilize a higher energy backlighter.

Fig. 3.7 shows the results of a finely resolved 2D simulation of an originally 3.5 mm wide screen opening using CTH. At the time of the snapshot the material jets are still ~2.5 mm apart, indicating that the screen opening needs to be of order 1 mm or wider to minimize the effects of jetting. Fig. 3.8 shows the expected transmission for 25 kV photons, indicating that reasonable transmission would be obtained for ~1 mm thick aluminum plasmas at densities near the critical point. Unfortunately, by the completion of this study the 25 kV backlighter was not available. When available it may be beneficial to perform experiments given the results of the gas cell experiments described in the next section.

4. Gas Cell Experiments

As mentioned above, it was apparent near the completion of this study that the 25 kV backlighter would not be available for use. We therefore had to alter the experimental plan and began a series of tamped release experiments. Fig. 4.1 shows the experimental configuration. In concept the only difference between the tamped release and full release is the presence of a low density gas behind the aluminum target. In practice this required the development of a gas cell capable of
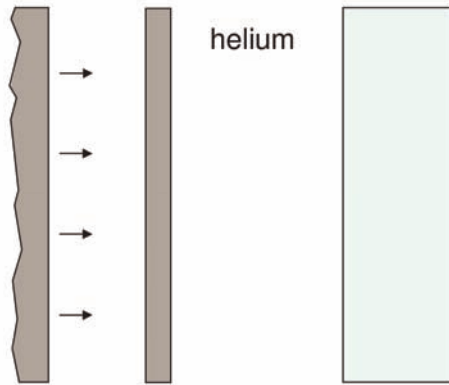
Figure 4.1. Experimental configuration for the gas cell experiments.

containing a gas within a vacuum environment. To accomplish this we leveraged previous work on liquid deuterium which also required a gas cell. The gas cell design is shown schematically in Fig 4.2. The front of the cell is comprised of an aluminum cup, while the rear of the cell is comprised of a quartz window. The window is clamped in place by the fiber optic probe holder. Indium wire was used as a means to provide a vacuum tight seal between the cell and the window.

One atmosphere of helium gas was used to tamp the aluminum release. This gas was chosen due to the low initial density. This results in a shock impedance low enough that release of aluminum from several 100 GPa resulted in a shocked state in the helium of between 1-2 kbar, pressures near the estimated pressure of the liquid-vapor critical point.

As in the case of the full release experiments, VISAR was used as a diagnostic to determine the response of the aluminum and helium gas. Experiments were performed for aluminum shocked states between ~475 GPa and ~1000 GPa. Raw VISAR data from one of these experiments, corresponding to ~475 GPa in the aluminum, is shown in Fig 4.3. Several events are evident in the raw data records. The signal changes dramatically upon traversal of the shock from the aluminum to the helium gas, which occurs in Fig. 4.3 at a time of ~230 ns. Approximately 40 ns later the shock wave reaches the quartz window. Roughly 5 ns later a second shock event at the helium/quartz interface occurs. Finally, at a time of ~350 ns the leading shock reaches the rear of the quartz window.

Similar data was obtained for a total of six experiments between 475 and 1000 GPa in the aluminum. Raw data for each of these experiments is shown in Fig 4.4. Both time shifts and baseline shifts were performed for clarity and to allow ease of comparison of transit times. Two trends are noticeable in this comparison. First, it is clear that the transit time of the shock wave across the cell monotonically decreases with increasing pressure in the aluminum targ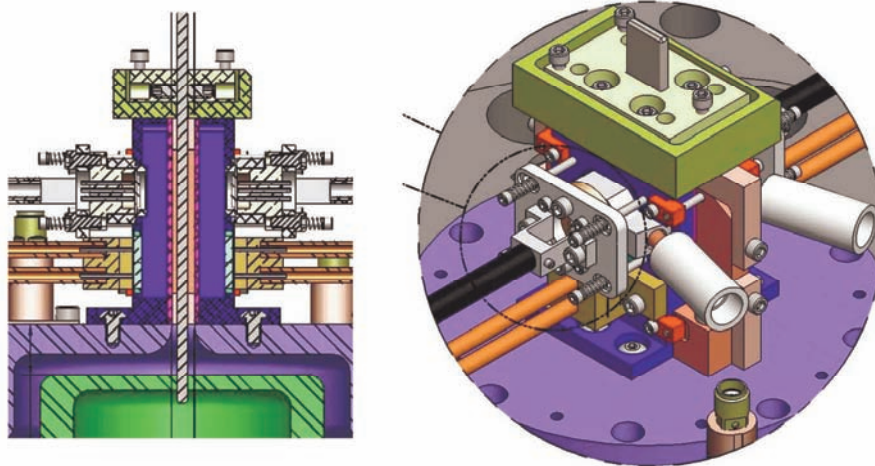et. However, it is also clear that this decrease in transit time is not linear; the decrease in time with increasing pressure is more rapid at lower pressures in the aluminum target, with

Figure 4.2. Schematic drawing of the gas cell experiment.

the change at higher pressures being significantly smaller. Second, the time interval between the two shock events at the helium/quartz interface, which we will refer to as a dwell time, also decreases with increasing pressure in the aluminum target. Furthermore, this dwell time appears to essential vanish for release from shocked states above ~750 GPa.

These trends are illustrated clearly in Fig. 4.4, which shows the helium shock velocity (blue diamonds) and the dwell time (pink squares) as a function of pressure in the aluminum target. The corresponding blue and pink lines in the figure are guides for the eye. Both features appear to show a marked change from linearity at a pressure of ~700-800 GPa.
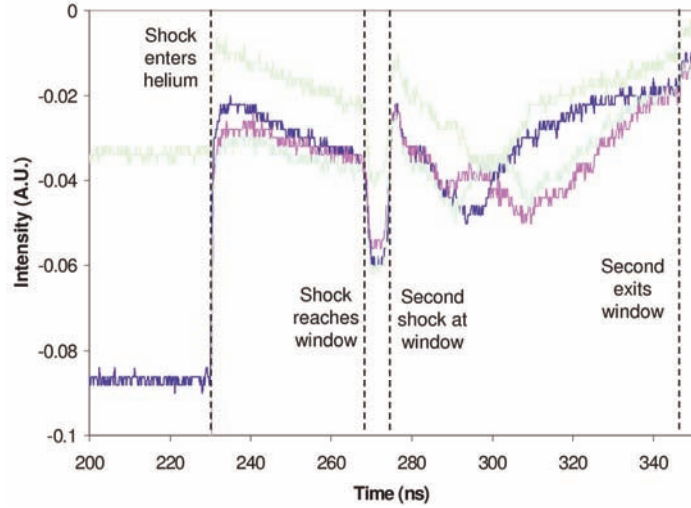

Figure 4.3. Raw VISAR data for a gas cell experiment at a pressure of ~475 GPa in the aluminum target. Several events are clearly observable in the VISAR data.

In an attempt to understand these results we performed several 1D simulations using CTH. The SESAME 5760 [13] model for helium was used along with both the SESAME 3700 and 3719 models for aluminum. As can be seen in the figure, reasonable agreement for the helium shock velocity is obtained for both aluminum EOS models at pressures at or below ~700- 800 GPa. Both the 3719 and 3700 models for aluminum predict a continuation of a linear increase in shock velocity to 1000 GPa in the aluminum target, in contrast to the observed break from linearity.
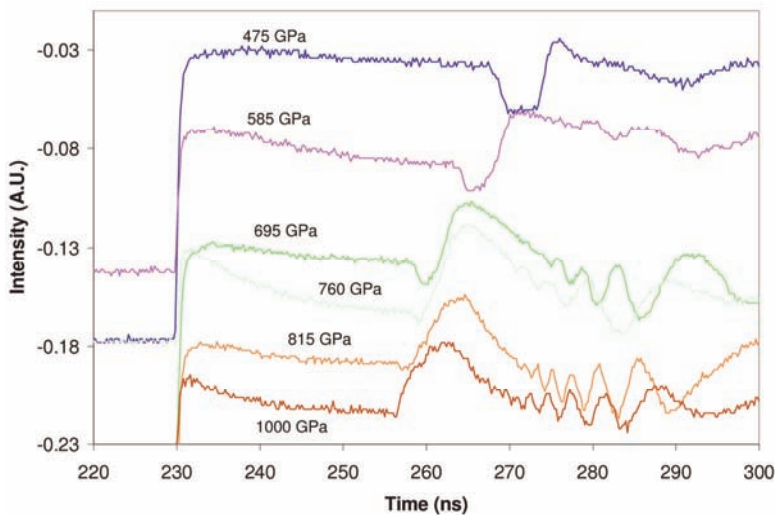

Figure 4.4. Raw VISAR data for a gas cell experiments at a pressures from ~475 to 1000 GPa.

At this point we do not fully understand these observations. However, we do believe that this is not the result of an experimental artifact. Fig. 4.5 shows the average shock velocity in the quartz window, determined from the measured transit time of the shock through the window, as a function of the pressure state in the aluminum target. Included in this figure are additional experiments performed on empty gas cells. It is clear from the figure that a linear trend is observed over the entire pressure range studied. This suggests that the observed break in linearity of the helium shock velocity is not an experimental artifact, but

rather is due to some change in the interaction of the aluminum releasing into the helium. At this point we speculate that this has something to do with the presence of the vapor dome, and may suggest that the release adiabat from a shocked state in aluminum near ~800 GPa skirts the critical point.

This speculation is supported by the predicted state of the aluminum at the interface between the aluminum and helium in the CTH calculations. The states reached in two simulations, corresponding to initial shocked states of ~500 and ~1000 GPa, are shown in Fig. 4.6

Figure 4.5. Helium shock velocity (blue diamonds) and dwell time (pink squares) as a function of the shocked state in the aluminum target. Also shown are calculated results for SESAME 3700 and 3719.

in pressure-density-temperature space. Each curve beginning at the Hugoniot, rapidly dropping in pressure, corresponds to a release adiabat from a state on the Hugoniot. In this plot the black curve that reaches the lowest pressure is a release starting at 200 GPa. Each subsequent curve begins at a Hugoniot state at a pressure of 100 GPa greater than the previous. Thus the two points reached in the simulations lie on release adiabats that start at ~500 and ~1000 GPa. The final states are in very close proximity to the predicted critical point for the 3719 EOS model. The band connecting these points represent the region accessed by the gas cell experiments performed, at least for the 3719 model.
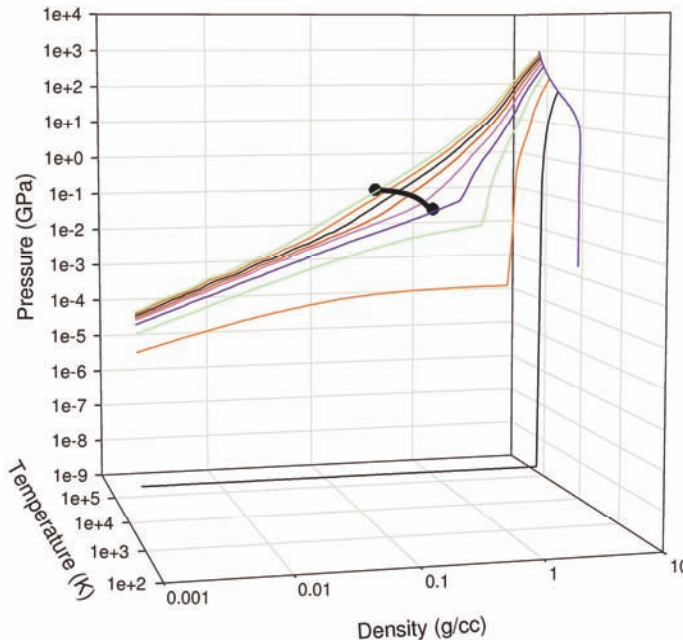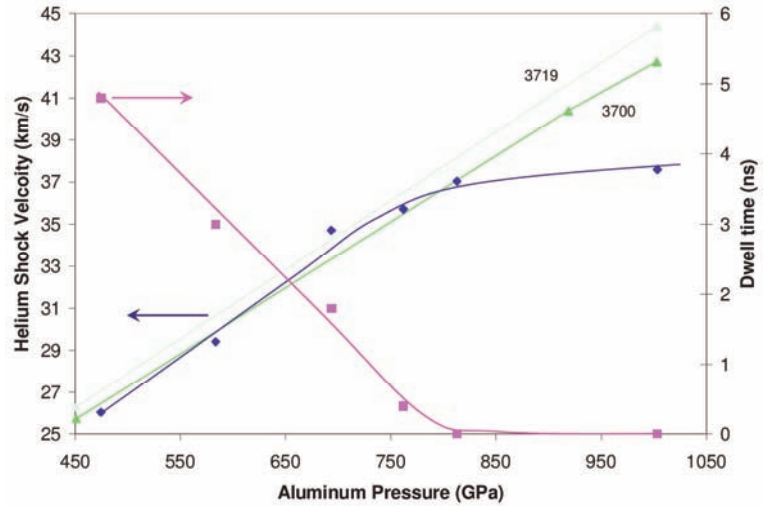

Figure 4.6. Release adiabats for SESAME 3719 in pressure, density, temperature space. The black points in the figure represent the states of the aluminum reached at the aluminum helium interface in the CTH calculations.

Given these calculations we can make some speculations regarding the location of the critical point for aluminum. In particular, the value of the helium shock velocity at the roll off seen in Fig 4.5 suggests a pressure state that is likely close to the pressure of the liquid-vapor critical point. Fig 4.7 plots the Hugoniot of helium in pressure versus shock velocity. This figure illustrates the stagnation pressures reached in the gas cell experiments. The lowest pressure experiment, in which the aluminum target

reached ~475 GPa, exhibited a helium shock velocity of ~26 km/s. This corresponds to a stagnation pressure of under 1 kbar (1 kbar = 0.1 GPa). The highest pressure experiments, in which the aluminum target reached ~700-1000 GPa, the helium shock velocities were between ~35-37 km/s. This corresponds to pressures of between ~1.7-2 kbar. This suggests that the critical point for aluminum is somewhere in the vicinity of ~2 kbar or less.

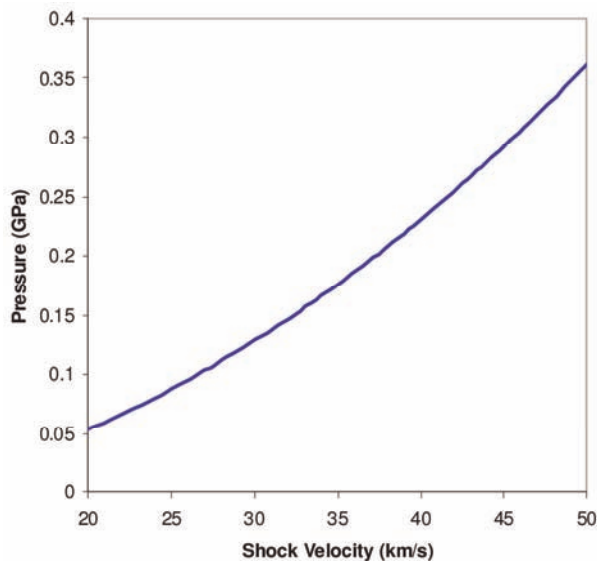# 5. Quantum Molecular Dynamics and QEOS Development

Figure 4.7. Hugoniot for helium.

A second aspect of this work was to develop a new equation of state (EOS) for aluminum. In order to develop a new EOS for aluminum, with comparable properties to SESAME 3700 in compression, but much improved treatment of expanded aluminum, we generated quantum molecular dynamics (QMD) calculations of the aluminum Hugoniot, principal isentrope, and several isotherms in the region of the liquid-vapor critical point. One isotherm in particular, 6000 K, shows the characteristics of the critical isotherm. This isotherm is plotted in Fig. 5.1.

Note the near vanishing of the derivative of the pressure with respect to density near 0.6 g/cc. This suggest that the 6000K isotherm comes very close to the liquid-vapor critical point. In particular, the spot of near zero derivative provides an estimate of the critical point. This corresponds to a pressure, density, and temperature of ~1.8 kbar, ~0.6 g/cc, and ~6000 K, respectively. This equation of state data was provided to Richard More for use in calibrating a new aluminum equation of state using an improved version of the quotidian equation of state (QEOS). In the process of attempting to tune the EOS data to the QMD data, it was clear that the existing liquid-vapor model in QEOS was inadequate for properly capturing the behavior of expanded aluminum in the liquid-vapor region.

Figure 5.1. QMD calculations of the 6000K isotherm for aluminum near the liquid-vapor critical point.
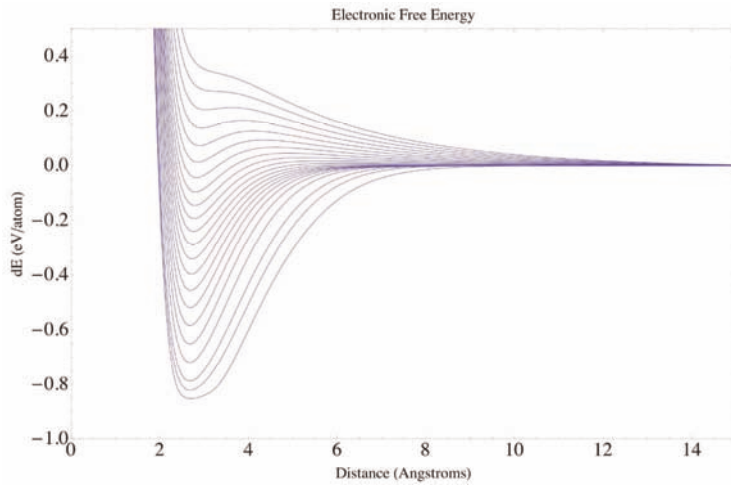
Figure 5.2. QMD calculations of the bond energy per atom of the aluminum-aluminum dimer as a function of atomic separation for various temperatures.

In order to better model the behavior of expanded aluminum, we also looked at the effect of finite electronic temperature in the aluminum-aluminum dimer potential. Fig. 5.2 shows the aluminum-aluminum bond energy per atom (total electronic free energy) as a function of the atomic separation. The curves correspond to 50K at the lowest level, followed by 500K, 1000K, and every next 1000 K up to 20000 K. Note the appearance of repulsion in the potential as the atoms begin to ionize. Richard More has developed a new approach to EOS modeling in the expanded regime using these temperature dependent pair potentials. An immediate benefit of this approach is that it is much easier to produce liquid-vapor critical points in the EOS that are more in line with the QMD calculations. The resulting EOS model developed using these QMD inputs is shown in Fig. 5.3. This model will be used for comparison with the experimental results of this study in the near future.

Independent of the development of a new equation of state, we also used the QMD calculations to estimate the Hugoniot state that would release to the critical point. Two release isentropes were calculated: one starting at 500 GPa and the other starting at 910 GPa. Both isentropes were calculated from the corresponding Hugoniot density at the particular pressures and temperatures down to near ambient density. The Gruneisen Γ along the release isentropes was found to be well approximated with a weak power law dependence. Once this power law dependence was
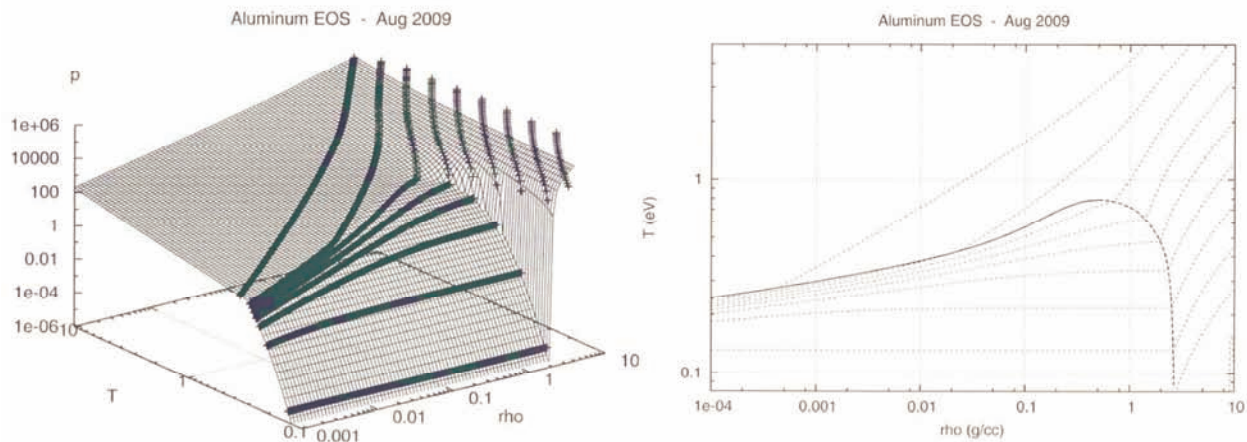

Figure 5.3. QEOS model developed in this study. Left panel shows the EOS surface and release adiabats in pressure, density, temperature space. Right panel shows projections of the release adiabats and the vapor dome in the temperature-density plane.

determined, we extrapolated down to the temperature and density of the QMD critical point, using interpolation for the isentrope parameters between 500 GPa and 910 GPa. This approximate analysis indicates that the critical isentrope intersects the Hugoniot in the vicinity of 700 GPa. We note that this treatment ignores distortions to the isentrope as the two phase region is approached, but existing EOS models suggest that this distortion is not significant for the critical isentrope. See for example the adiabat that intersects the vapor dome near the peak in Fig 5.4. This adiabat does not appear to exhibit the "repulsion" of the near by adiabats as the vapor dome is approached.

6. Future Work

Two more gas cell experiments are planned for this fiscal year, but will not be completed until after the writing of this report. The intent of these experiments will be to fill in critical gaps in the initial Hugoniot states of the aluminum target. Specifically, one experiment will be performed at an aluminum pressure of ~650 GPa, while the second will be performed at an aluminum pressure of ~900 GPa. These experiments should confirm the trend observed in the previous gas cell experiments, providing more confidence in observations which may indicate release to the critical point.

Obviously more work is needed to gain a better understanding of the experimental observations. While the possible indication of release to the critical point is exciting, it should also be viewed with caution. Further hydrocode simulations using the existing SESAME and the newly developed QEOS should be performed. However, one failing of these EOS models is the in ability to explicitly treat two phases. Maxwell constructions are used in the models in an attempt to treat the two phase region of the vapor dome. However, this has been shown to be inadequate in certain applications, which almost certainly includes the application described here. Thus it may be necessary to explicitly treat the two phases in a more complicated fashion to be able to make better contact with the experimental observations.

We have not had time to perform a detailed comparison of the most recent QEOS model for aluminum with the experimental results. However, initial comparison of this model with the QMD generated Hugoniot and critical release adiabat suggests that there may be need for further improvement of the QEOS model. We plan to continue working closely with Richard More on the continued development and implementation of the QEOS model. Given that this model is the most finely resolved of all the available aluminum EOS models in the vicinity of the critical point means that this EOS model will be invaluable in continuing the analysis of the experimental results.

It is unfortunate that the 25 kV backlighter was not available during this study. Work is continuing on the development of this diagnostic for use in Z experiments. When it does become available it would be very beneficial to perform at least a few experiments using this capability for release from states just above and just below ~700 GPa. Based on the results of the gas cell experiments, we would expect to see a qualitative change in the density profile of the expanding aluminum for these initial pressures.

If substantiated, this work would represent the first experimental evidence of the location of the critical point in aluminum. It would also provide a methodology of experimental determination of the critical point of a material of interest. Subsequent experimental campaigns could then be performed on materials of interest to various Sandia related missions; in particular the critical point for tungsten, a material commonly used in wire arrays for Inertial Confinement Fussion applications, could be identified.

References

1. K.S. Holian, Los Alamos Scientific Laboratory Report No. LA-10160-MS, 1984.

2. G.I. Kerley, Int. J. Impact Eng. **5**, 441 (1987).

3. S.L. Thompson, Sandia National Laboratories Report No. SAND89-2951, 1990.

4. S.D. Crockett, Los Alamos Report No. LA-UR-04-6442.

5. M.D. Knudson, R.W. Lemke, D.B. Hayes, C.A. Hall, C. Deeney, and J.R. Asay, J. Appl. Phys. **94**, 4420 (2003).

6. M.D. Knudson, J.R. Asay, and C. Deeney, J. Appl. Phys. **97**, 073514 (2005).

7. L.M. Barker and R.E. Hollenbach, J. Appl. Phys. **43**, 4669 (1972).

8. A.A. Bakanova, I.P. Dudoladov, M.V. Zhernokletov, V.N. Zubarev, and G.V. Simakov, J. Appl. Mech. Techn. Phys. **24**, 204 (1983).

9. B.L. Glushak, A.P. Zharkov, M.V. Zherokletov, V.Y. Ternovoi, A.S. Filimonov, and V.E. Fortov, Sov. Phys. JETP **69**, 739 (1989).

10. I.V. Lomonosov, V.E. Fortov, K.V. Khishchenko, and P.R. Levashov, in *Shock Compression of Condensed Matter – 2001*, edited by M.D. Furnish, N.N. Thadani, and Y. Horie (AIP, New York, 2002).

11. R. More, equation of state from this work.

12. D.B. Sinars, M.E. Cuneo, G.R. Bennett, D.F. Wenger, L.E. Ruggles, M.F. Vargas, J.L. Porter, R.G. Adams, D.W. Johnson, K.L. Keller, P.K. Rambo, D.C. Rovang, H. Seaman, W.W. Simpson, I.C. Smith, and S.C. Speas, Rev. Sci. Instrum. **74**, 2202 (2003).

13. Lawrence Livermore National Laboratory Report No. UCIR-740, 1974.

Distribution

1   MS0899   Technical Library, 9536

Sandia National Laboratories